ACS Combinatorial Science

Research Article

pubs.acs.org/acscombsci

Mapping Structure-Composition-Property Relationships in V- and Fe-Doped $LiMnPO_4$ Cathodes for Lithium-Ion Batteries

Ian D. Johnson,[†] Melanie Loveridge,[‡] Rohit Bhagat,[‡] and Jawwad A. Darr*[,†]

[†]Department of Chemistry, University College London, 20 Gordon Street, London WC1H 0AJ, U.K.

[‡]Warwick University, Coventry, U.K., CV4 7AL

Supporting Information

ABSTRACT: A series of $LiMn_{1-x-y}Fe_xV_yPO_4$ (LMFVP) nanomaterials have been synthesized using a pilot-scale continuous hydrothermal synthesis process (CHFS) and evaluated as high voltage cathodes in Li-ion batteries at a production rate of 0.25 kg h^{-1}. The rapid synthesis and screening approach has allowed the specific capacity of the high Mn content olivines to be optimized, particularly at high discharge rates. Consistent and gradual changes in the structure and performance are observed across the compositional region under investigation; the doping of Fe at 20 at% (with respect to Mn) into lithium manganese phosphate, rather than V or indeed codoping of Fe and V, gives the best balance of high capacity and high rate performance.

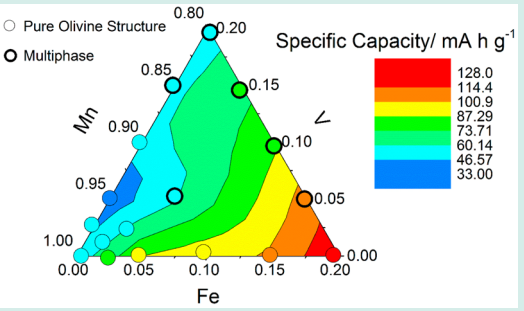

KEYWORDS: *lithium-ion battery, doped LMP, continuous hydrothermal synthesis, high energy, cathode*

INTRODUCTION

Lithium-ion batteries (LIBs) currently offer the highest energy densities of all commercial rechargeable battery technologies. Current cathode technology in LIBs relies largely on cobalt oxide-based materials, and there has been much interest focused on developing more inexpensive and sustainable materials composed principally of less toxic metals. The olivine family of materials (especially $LiMPO_4$, where M = Fe, Mn, or others) have been heavily researched as candidate Li-ion battery cathodes because of their reasonable theoretical capacity (170 mA h g^{-1} for $LiFePO_4$), thermal stability, environmental inertness and high cycle life.[1]

$LiMnPO_4$ (LMP) is of interest as a higher energy density cathode compared with $LiFePO_4$ (LFP) [theoretical energy density value of 697 for LMP vs 586 W h kg^{-1} for LFP]. This difference is due to the higher potential of the Mn^{2+}/Mn^{3+} couple compared with the Fe^{2+}/Fe^{3+} (4.1 V vs Li/Li^+ as opposed to 3.45 V vs Li/Li^+).[2] However, LMP has lower electronic conductivity than LFP (10^{-10} S cm^{-1} for LMP compared to the range ~10^{-7} to 10^{-10} S cm^{-1} for LFP).[3] There are also electron−lattice interactions in LMP (from the Jahn−Teller effect), which causes significant lattice deformations,[4] thereby limiting its achievable capacity and cyclability.[5] Manganese dissolution in the electrode has also been reported as an issue during operation, leading to Mn plating onto the Li anode and a decline in electrochemical performance.[6] For these reasons, the electrochemical performance of pure (undoped) LMP is very much limited, and generally requires a higher proportion of conductive carbon in the electrode compared to LFP (>20 wt%) or nanosizing the particles or carbon coating particle surfaces to attain significant reversible Li^+ intercalation. Rangappa et al. reported a specific capacity of 153 mA h g^{-1} at a discharge rate of C/100 and a value of 62 mA h g^{-1} at 0.5 C for LMP made via a liquid phase batch process.[7] Wang et al. achieved a specific capacity of 145 mA h g^{-1} at a discharge rate of C/20 and a value of 113 mA h g^{-1} at 1 C for LMP made using a batch polyol synthesis method.[8] More recently, Zheng et al. reported a specific capacity of 152 mA h g^{-1} at C/20 and 60 mA h g^{-1} at 5C,[9] using a solid state synthesis route from a mixture of Mn_2O_3 and MnO_2. Yoo et al. synthesized 3D macroporous $LiMnPO_4$ flakes via a colloidal template, which when tested as a cathode achieved 162 mA h g^{-1} at C/10 and 110 mA h g^{-1} at 10C.[10] All of the aforementioned electrodes contained a high proportion of carbon (generally 17 wt% or more), significantly reducing tap density and therefore, reducing the likelihood for commercial development. Kwon et al. achieved a capacity of 165 mA h g^{-1} at C/40 and 66 mA h g^{-1} at 1C with an electrode with only 10 wt% carbon content.[11] Clearly, the literature shows that pure LMP as a cathode material is limited, particularly at high C rates.

Doping LMP with transition metals is a promising approach to improve electrochemical performance. Doping with cations of oxidation states >2+ also brings the potential advantage of generating Li^+ vacancies as a charge-compensation mechanism, and is a well-established method of improving the performance of both LFP and LMP.[12] It has been observed that replacing the manganese ion with another divalent cation (such as Zn^{2+}, Mg^{2+}, or Fe^{2+}), leads to improved capacity retention at high discharge rates, which was attributed to increased electronic conductivity and reduced particle size.[12] Martha et al.

Received: March 14, 2016
Revised: August 1, 2016
Published: September 15, 2016

DOI: 10.1021/acscombsci.6b00035
ACS Comb. Sci. 2016, 18, 665−672

developed $LiMn_{0.8}Fe_{0.2}PO_4/C$ cathodes, which achieved a specific capacity of 162 mA h g^{-1} at C/10 and >90 mA h g^{-1} at 10C.[13] Furthermore, Sun et al. developed micron-sized $LiMn_{0.85}Fe_{0.15}PO_4$ with a high volumetric capacity of 370 mA h cm^{-3}.[14]

As well as LMP, LFP has also been doped with transition metals, such as V, resulting in dramatic improvements in high-rate performance, either because of favorable structural changes in the olivine lattice/improvements in conductivity or due to the formation of highly conductive secondary vanadium-containing phases on the LFP surface.[15−19] The latter approach has also been used to improve the performance of LMP cathodes in a Li-ion battery, by formation of a V-doped $LiMnPO_4$ material or a composite cathode comprising of a highly conductive $Li_3V_2(PO_4)_3$ phase mixed with LMP.[20−22]

The majority of syntheses of LFP and LMP in the literature consist of batch solid-state or hydrothermal or wet chemical methods.[9,21,23−25] Solid-state methods to make such materials into high performance cathodes usually involve high temperatures, lengthy heat-treatments and multiple processing steps, including grinding.[9,21] In contrast, batch hydrothermal reactions typically require lower synthesis temperatures while often needing to incorporate surfactants to reduce particle size and control morphology, all of which adds additional cost and complexity to the process. Such methods also suffer from batch-to-batch variations and are challenging to scale-up.

Continuous hydrothermal flow synthesis (CHFS) methods possess some advantages compared to batch-type synthesis routes, as continuous processes are often more flexible and can allow independent control over reaction variables (such as pressure, reaction temperature and residence time). Furthermore, the CHFS process can convert solution precursors to solid products (dispersed in the process liquid) over timescales of a few seconds, often generating kinetic (metastable) products. With CHFS methods, this rapid conversion to products (typically <1 s) is achieved by mixing aqueous metal salts at room temperature with a flow of supercritical water (in a well-defined mixer arrangement, Figure S1−2), rapidly forming nanoparticles via simultaneous hydrolysis and dehydration.[26,27]

The speed and simplicity of CHFS, has led to the development of high throughput continuous hydrothermal routes for rapid manufacture of libraries of nanomaterials, to allow exploration of structure−property-compositional relationships.[28−32] The approach was previously successful in the production of large or partial phase diagrams for nanomaterials, such as the Ce−Zr−Y−O and Ce−Zn−O systems.[28−30] Using a similar rapid synthesis approach, libraries of doped nanomaterials were developed, for example, ZnO[31] and Zn−Ti oxide photocatalysts,[32] and Eu-doped yttria phosphors.[33] In addition to the direct synthesis of nanomaterials libraries, high-throughput CHFS was used to make nanocoprecipitated oxides, used as precursors for the direct solid state (heat-treat with no grinding) synthesis of complex oxide libraries, for example, doped $La_4Ni_2FeO_{10-\delta}$ mixed ion conductors.[34] In many of these reports, the use of fast screening or parallel testing methods were used to quickly develop structure−property-composition relationships for the nanomaterials/products.

Historically, continuous hydrothermal processes have largely been used to investigate the production of metal oxides. More recent work has begun to explore sulfides,[35] and also phosphates.[27,36−38] To the best of the author's knowledge, there are no peer-reviewed reports of continuous hydrothermal flow synthesis of LMP or its doped analogues, although LFP has been reported with varying degrees of performance as a Li-ion battery cathode.[39−41]

A series of $LiMn_{1-x-y}Fe_xV_yPO_4$ (LMFVP) nanomaterials were synthesized using a pilot-scale CHFS process in an attempt to optimize the specific capacity within compositions with high Mn content, and enable comparisons between the merits of the two dopants.

RESULTS AND DISCUSSION

Herein, we report the synthesis of LMP and the manganese-rich region of the $LiMn_{1-x-y}Fe_xV_yPO_4$ phase diagram (as highlighted in Figure 1a). Pure $LiMnPO_4$ and the Fe- or V-doped variants (with nominal compositions shown in Figure 1b) were all synthesized with an amorphous carbon coating using a pilot-plant CHFS process.[26] The rapid formation of a large number of samples (17) in the phase-space allowed the comparison of structure and performance, which has not previously been achieved for these compounds. The pure $LiMnPO_4/C$ sample was named LMP, and the iron/vanadium-doped samples (also coated with amorphous carbon) were named LMFVP(x,y), where x and y are the nominal percentages of iron and vanadium, respectively (as a proportion of total transition metal content). The nominal content refers to the metal at% present in the precursors, normalized to a total of 100%. These samples were all heat-treated (to graphitize the carbon coatings) to give the corresponding samples named ΔLMP and ΔLMFVP(x,y). The as-prepared samples after freeze-drying were generally fine gray-blue or gray-pink powders, and heat-treatment of these samples, gave black powders. The properties of the surface carbon was analyzed using Raman spectroscopy for both the as-prepared and heat-treated samples. Prior to heat-treatment, a very broad feature in the range 200−2000 cm^{-1} was observed, corresponding to a high proportion of disordered carbon, although some graphitic sp^2 carbon was evident from the presence of the G band (Figure S3). Analysis of the samples after heat-treatment confirmed the conversion of the carbon coating to a graphitic carbon coating, with only the characteristic D and G bands observed (Figure S4). The small feature observed at 950 cm^{-1} was consistent with the symmetric stretching vibration of PO_4.

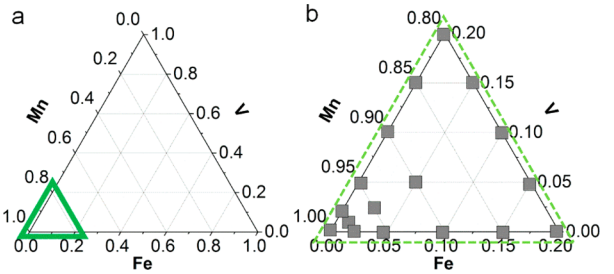

Figure 1. (a) Overall phase diagram of $LiMn_{1-x-y}Fe_xV_yPO_4$, with the area for investigation highlighted with a green triangle, and (b) the nominal composition of all samples synthesized within the area of interest (gray squares indicate nominal sample composition).

Powder X-ray diffraction (XRD) patterns of the as-prepared samples all exclusively showed the pure olivine $LiMnPO_4$ structure (good match to JCPDS reference pattern number 00-077-0178, Figure S5a−c). Significant peak-shift and broadening was observed in the as-prepared olivine structures as the

DOI: 10.1021/acscombsci.6b00035
ACS Comb. Sci. 2016, 18, 665−672

vanadium levels increased, which may be indicative of increasing lattice strain, and comparatively reduced shift (with no broadening) was observed with increasing Fe content (Figure S5b and d). There was consistent variation in the lattice parameters and unit cell volume with composition, as shown in Figure 2a–d and Table S2, calculated from LeBail fits of the

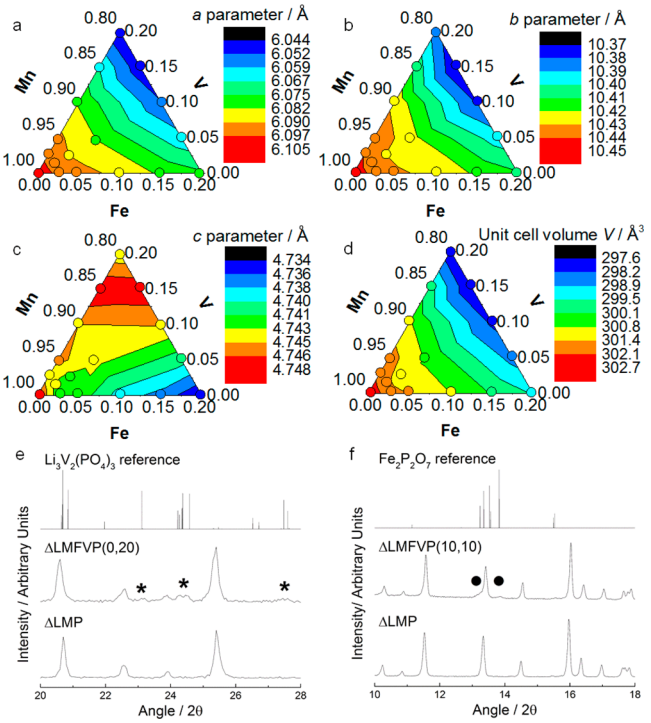

Figure 2. Heat-maps of the lattice parameters of the as-prepared LMFVP samples with (a) the *a* parameter, (b) the *b* parameter, (c) the *c* parameter, and (d) the unit cell volume, *V*. The impurity phases in samples are indicated in the following XRD patterns: (e) $Li_3V_2(PO_4)_3$ impurity peaks (*) in sample ΔLMFVP(0,20) (Cu Kα radiation) and (f) weak and broad minor peaks (●) assigned as $Fe_2P_2O_7$ in sample ΔLMFVP(10,10) (Mo Kα radiation).

X-ray Diffraction patterns (Figures S6–22). It can be seen that increasing Fe and V dopant levels led to a smooth reduction of the *a* and *b* lattice parameters, whereas the V dopant had the most significant effect on the *c* parameter, with increased V substitution increasing the *c* parameter across all compositions. This is consistent with the distortion observed with V substitution in LFP by the authors and others, and implies successful incorporation of V into the olivine structure, which is still a matter of some debate in the literature.[18,42,43] This systematic change in parameters could only be observed due to the wide phase-space observed and the number of samples analyzed.

The samples were all heat-treated to graphitize the carbon and remove any antisite defects. However, a limitation in vanadium solubility after heat-treatment was observed, with an $Li_3V_2(PO_4)_3$ impurity phase forming for certain dopant levels as shown in the XRD patterns (Figure 2e, Figure S5e and f). Interestingly, the additional presence of iron in the V-doped LMP samples biased the formation of a different impurity phase, $Fe_2P_2O_7$, compared to the samples doped with V only (Figure 2f, Figure S5f). The location of the two weak and broad peaks at 13.2 and 13.8° in 2θ, resulted in a tentative assignment for the iron pyrophosphate ($Fe_2P_2O_7$) phase (match to JCPDS reference pattern number 00-076-1672). This result was somewhat surprising, as it suggests the iron dopant was less stable in the structure than vanadium in these materials. The presence of aliovalent dopants in the olivine structure has traditionally been discounted,[43] although there is an increasing body of evidence that aliovalent doping is possible in both $LiFePO_4$ and $LiMnPO_4$.[16,18,20,42,44] Indeed, the high doping degree achieved in sample LMFVP(0,20) has not been achieved for LMP previously, and indicates the phase was only accessible due to the relatively low synthesis temperature used herein (335 °C) and rapid conversion from precursor to product in the process.

Field-emission scanning electron microscope (FE-SEM) images of selected heat-treated samples showed they consisted of fused networks of agglomerated particles approximately 100 nm in size (Figure 3). A significant amount of faceting was observed in sample ΔLMFVP(20,0), which appeared cuboid-like, and may reflect changes in the surface energies of the samples with doping. The small particle size achieved herein reflected the high degree of supersaturation and rapid nucleation achieved when the precursors were combined with supercritical water in CHFS.

The heat-treated samples were made into electrodes in Li-ion coin half-cells and cyclic voltammetry (CV) tests were conducted at a scan rate of 0.5 mV s^{-1}. The Mn^{2+}/Mn^{3+} couple at 4.1 V vs Li/Li^+ was observed in all cases (Figure 4, Figures S23–35) and clear trends were observed for the doped samples; for the samples in the binary transition metal phosphate system of ΔLMP to sample ΔLMFVP(20,0), the gradual emergence of the Fe^{2+}/Fe^{3+} couple was observed as iron content increased. Crucially, the peak current of the Mn^{2+}/Mn^{3+} couple increased with increasing iron dopant, suggesting that the kinetics of lithiation were improved by iron doping (Figure 4a, Figure S23–35). For samples ΔLMFVP(0,20) and ΔLMFVP(5,15), the emergence of current peaks at 3.6, 3.7, and 4.1 V was attributed to the minor $Li_3V_2(PO_4)_3$ phase, which was formed upon heat-treatment of those samples (Figure 4b, Figure S32). There was very little change in the current peak intensity of the Mn^{2+}/Mn^{3+} couple with V content, implying the V dopant had a smaller effect on performance compared to doping of Fe (Figure 4b, Figure S23–35). The mixed Fe/V doped samples LMFVP(*x*,*y*) (where *x* = *y*) showed no indication of any significant additional redox activity due to the minor $Fe_2P_2O_7$ phase (Figure 4d, Figure S23–35).

The Fe-doped samples generally exhibited significantly better rate capability in constant-current constant-voltage tests compared with the pure ΔLMP sample. In contrast, V-doping was found to have less influence on cathode performance (Figure 5, Table S3). The heat map of the sample capacities generated at C/2 and 5C, respectively, showed the dominant beneficial effect of iron doping on the discharge capacity of LMFVP. This was surprising given the well-documented apparent positive effect of the inclusion of V in the olivine lattice or the presence of a $Li_3V_2(PO_4)_3$ conductive impurity.[20−22] However, the ratio $Li_3V_2(PO_4)_3$:$LiMnPO_4$ was lower in this study (maximum possible was 1:8 for $Li_3V_2(PO_4)_3$:$LiMnPO_4$) than those typically reported in the literature (that are typically 1:4),[21,22] and could explain this apparent contradiction. To our knowledge, this is the first combinatorial analysis of two beneficial dopants in the nanoparticle $LiMnPO_4$ system to give an accurate comparison.

DOI: 10.1021/acscombsci.6b00035
ACS Comb. Sci. 2016, 18, 665–672

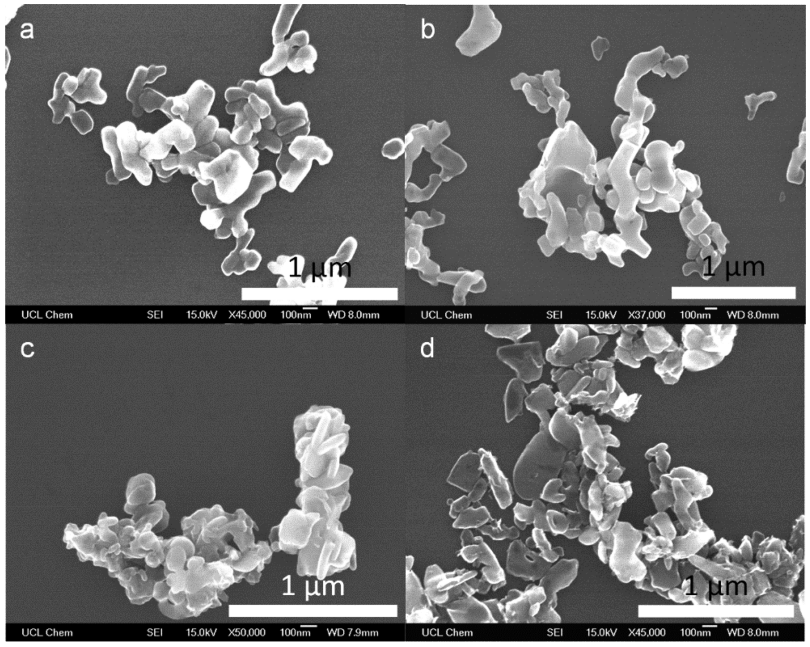

Figure 3. SEM micrographs of (a) LMP, (b) LMFVP(20,0), (c) LMFVP(0,20), (d) LMFVP(10,10).

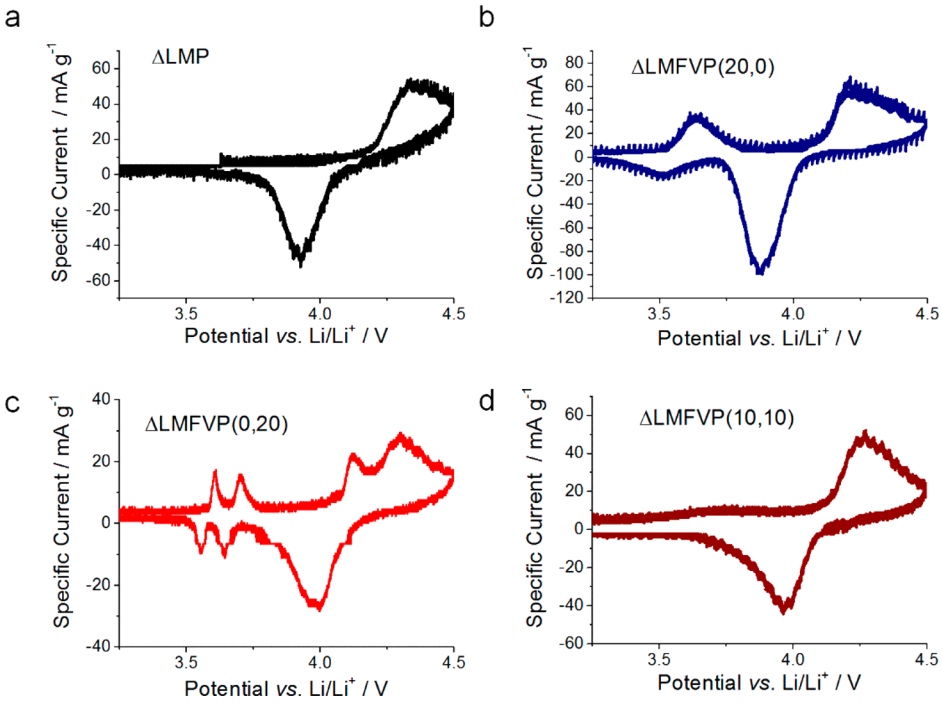

Figure 4. Cyclic voltammetry of heat-treated olivine nanomaterials made into Li-ion cathodes: (a) ΔLMP, (b) ΔLMFVP(20,0), (c) ΔLMFVP(0,20), and (d) ΔLMFVP(10,10) at a scan rate of 0.05 mV s^{-1}.

The performance of the $LiMn_{0.8}Fe_{0.2}PO_4$ cathode at a 5C charge/discharge rate was superior compared with other Fe-doped samples herein at this C rate, and achieved a discharge capacity of 85 mA h g^{-1} (Figure 6), and maintained a stable discharge capacity of 125 mA h g^{-1} at C/2. This trend was reflected in the energy densities achieved by the samples (Table 1), where a smooth increase was observed with increasing Fe content. The improvement in high power performance, can be attributed to an increase in bulk electronic conductivity as suggested by others,[5] and also reduced strain in the delithiated olivine structure due to the reduced presence of Jahn−Teller distorted Mn^{3+} ions, when the Mn is partially substituted with Fe.[5,12] While the proportion of carbon in the electrode was still too high compared to a commercial electrode (15 wt% overall), this is still comparatively low compared to similar LMP based materials in literature.[7,8,45] Combined with the semi-industrial scale of synthesis of these materials, the performance detailed herein for the best doped LMP samples represents a step forward in the development of $LiMnPO_4$ cathodes. Long-term cycling tests indicated reasonable stability of the material, with 70% capacity retention over 200 cycles at C/10 (Figure S36). A Coulombic efficiency of 98% was also observed, implying minor

DOI: 10.1021/acscombsci.6b00035
ACS Comb. Sci. 2016, 18, 665−672

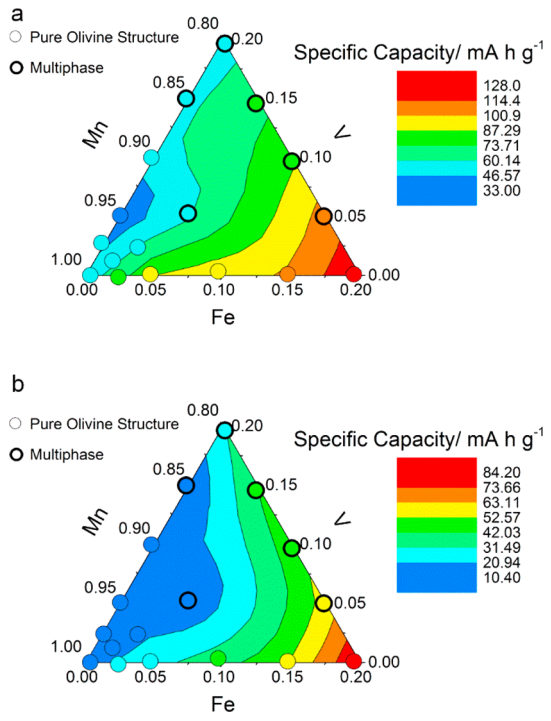

Figure 5. Heat-maps of specific capacity values for half-cell Li-ion coin cells made from the heat-treated nanomaterials in the Mn-rich corner of the ΔLMFVP phase diagram when charged/discharged at (a) C/2 and (b) 5C. Bolded open circles represent samples that have slightly phase separated after heat-treatment and normal open circles are still phase pure. The cell with sample ΔLMFVP(20,0) displayed the highest specific capacities (at charge/discharge rates of C/2 and 5C, respectively).

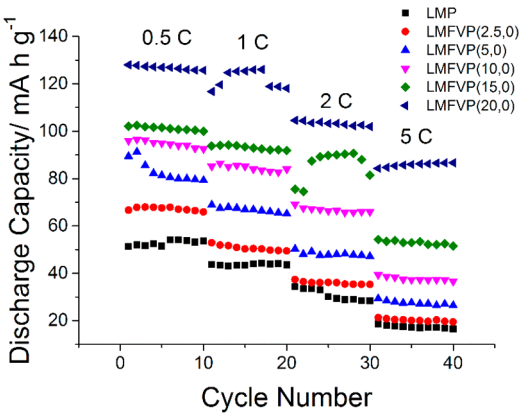

Figure 6. Cycling performance of the Fe-doped LMP family of cathode materials at different C rates.

electrolyte degradation due to the high charge voltage (4.5 V) used.

CONCLUSIONS

A high-throughput nanomaterials synthesis approach was taken to develop high-performance carbon-coated LMFVP cathodes via a continuous hydrothermal pilot-scale process. The effect of vanadium and iron dopants were investigated across part of the tertiary phase diagram for the heat-treated olivines, where the iron dopant had the most beneficial effect on improving electrochemical performance. The combination of carbon-coating, nanosizing and iron doping gave an optimized cathode material of $LiMn_{0.8}Fe_{0.2}PO_4$, which achieved a reversible specific discharge capacity of 85 mA h g^{-1} at a high discharge rate of 5C. This was comparable to the best performances achieved in the academic literature for similar materials, especially given the low carbon content (15 wt% C) of the electrode. Importantly, the materials herein had the advantage that they were synthesized on a pilot-plant at process at a production rate of 0.25 kg h^{-1} rather than grams per day as demonstrated by the comparable literature, which offers potential for further scale-up and investigation of even larger cell formats or packs in the future.

Table 1. Theoretical and Average Energy Densities (from 10 Cycles) of LMP and the Fe-Doped Samples at Discharge Rates of C/2 and 5C in the Potential Window 2.0−4.5 V versus Li/Li$^+$[a]

sample	theoretical energy density (W h kg^{-1})	Obs. ED (W h kg^{-1}) C/2	Obs. ED (W h kg^{-1}) 5C	discharge capacity at C/2 (mA h g^{-1})
ΔLMP	697	182	51	52
ΔLMFVP(2.5,0)	694	229	57	68
ΔLMFVP(5,0)	691	285	79	91
ΔLMFVP(10,0)	686	322	102	96
ΔLMFVP(15,0)	680	348	149	102
ΔLMFVP(20,0)	675	453	254	127

[a]Discharge capacities at C/2 are included for comparison. Obs. ED = observed energy density.

EXPERIMENTAL PROCEDURES

Carbon-coated iron- and vanadium-doped lithium manganese phosphate samples (where the C was amorphous in the as-prepared material) were synthesized using a pilot-scale CHFS reactor utilizing a patented confined jet mixer (CJM). A detailed description of the pilot-scale process can be found elsewhere, and a schematic is provided in the Supporting Information (Figure S1).[25]

The CHFS process for making nanomaterials can be summarized as follows: the precursors were prepared in two aqueous solutions. The first aqueous solution consisted of the following metal salts in the desired ratio; $MnSO_4{\cdot}H_2O$ (99+ %, Sigma-Aldrich, Steinheim, Germany), $FeSO_4{\cdot}7H_2O$ (99+ %, Alfa Aesar, Heysham, UK), $VOSO_4{\cdot}5H_2O$ (17−23% V, Acros Organics, Loughborough, UK), 0.375 M H_3PO_4 (85−88 wt%, Sigma-Aldrich, Steinheim, Germany), and fructose (99%, Alfa Aesar, Heysham, UK) in deionized (D.I.) water. The composition of this solution was varied such that the sum of [Mn], [Fe] and [V] was 0.25 M and the concentration of fructose was fixed throughout at 0.65 M (described in full in Table S1). The second solution used in the process contained 0.8625 M $LiOH{\cdot}H_2O$ (99+ %, Fischer Scientific, Loughborough, UK) in D.I. water for all experiments.

Both the metal salt and LiOH solutions were pumped to meet in a T-piece mixer (0.25 in. internal diameter) with 200 mL min^{-1} flow rate each. This combined mixture thus had a total flow rate of 400 mL min^{-1} and this was then delivered into the sidearms of the confined jet mixer (CJM, Figure S2), where it rapidly mixed with a flow of supercritical water at 450 °C and 24.1 MPa (flow rate of 400 mL min^{-1} for this water when it was under ambient conditions) to give reaction temperature of ∼335 °C under highly turbulent conditions (the design of the CJM is in the Supporting Information and is described fully

DOI: 10.1021/acscombsci.6b00035
ACS Comb. Sci. 2016, 18, 665−672

elsewhere).[25] The nanoparticles formed in or near the CJM exit had a residence time of ~6.5 s before passing through a pipe-in-pipe countercurrent heat exchanger and being cooled to near ambient temperature. The cooled slurry then passed through a back-pressure regulator (Swagelok KHB Series) which maintained the system pressure at 24.1 MPa, after which it was collected in a plastic container open to the atmosphere.

The slurry settled after 1 h and the supernatant (containing unreacted precursors and byproducts) was siphoned off. The slurry was concentrated further using centrifugation (1500 rpm for 5 min), and the resultant wet paste was dialyzed in D.I. water until the conductivity of the liquid reduced below 150 μS. The cleaned paste was further concentrated with centrifugation (4500 rpm over 30 min) to give a clean, wet product, which was frozen and freeze-dried by slowly heating from −60 to 25 °C, over 24 h under vacuum of <13 Pa. The freeze-dried powder was subsequently heat-treated from ambient temperature up to 700 °C (held for 3h at this temperature), with a heating rate of 5 °C min^{-1} under a flow of argon.

Powder XRD patterns were obtained on a Bruker D4 Endeavor diffractometer using Cu Kα radiation (λ = 1.54 Å) in the 2θ range 5 to 60° with a step size of 0.05° in 2θ and a count time of 4 s. LeBail analysis was performed using MAUD (Material Analysis Using Diffraction) software.[46] In addition, the $Fe_2P_2O_7$ impurity phase was identified using Mo−Kα radiation (λ = 0.71 Å) over the 2θ range 10−18° with a step size of 0.5° and step time of 20 s. The size and morphology of the heat-treated particles were determined by FE-SEM.

Raman spectra were collected on a Raman microscope system with a laser excitation wavelength of 514.5 nm; the laser power was set to 10% of full power for all samples. Scans were collected in the range 200−2000 cm^{-1}; each individual scan lasted 30 s, and the sum of 4 individual scans were combined to give the final spectrum (total scan time of 2 min).

The Li-ion battery cathodes were prepared by mixing each heat-treated sample with conductive agent (carbon black, Super P, supplied by Alfa Aesar, Heysham, UK) and polyvinylidene fluoride, PVDF (PI-KEM, Staffordshire, UK) in such a way as to give an active material/carbon/binder dry mass ratio of 75:15:10 for all electrodes (inclusive of surface carbon from the synthesis and heat-treatment, which was in the range 2.5 to 6.3 wt% of the overall mass of the heat-treated samples) (Table S1). To make inks, the PVDF was stirred in *N*-methyl-2-pyrrolidone, NMP (>99.5%, Sigma-Aldrich, Steinheim, Germany) for at least 1 h at room temperature until it was fully dissolved. This solution was combined with the heat-treated sample and conductive agent and ball-milled for 1 h; the resulting slurry was cast on aluminum foil (PI-KEM, Staffordshire, UK) and dried in an oven at 70 °C. 16 mm diameter circular electrodes were punched out and pressed with a pressure of 1.5 tons cm^{-2}. The mass loadings for all electrodes were in the range 2.3 to 2.7 mg cm^{-2}.

Two electrode 2032-type coin cells (Hohsen, Japan) were used to conduct electrochemical experiments, and were assembled in a dry room with a dew point of <−40 °C. Lithium metal foil was used as the counter electrode (PI-KEM, Staffordshire, UK), and the separator (Celgard) was saturated with an organic electrolyte (1 M $LiPF_6$ in 1:1 ethylene carbonate/ethyl methyl carbonate, with 1 wt% vinylidene carbonate additive, supplied by BASF, Ludwigshafen, Germany).

Electrochemical measurements were performed using an Arbin Instruments battery tester at 20 °C. The electrochemical performance was investigated by cyclic voltammetry in the range from 2.0 to 4.5 V vs Li/Li^+ at a scan rate of 0.05 mV s^{-1}. Galvanostatic charge/discharge cycling tests (specific current tests) were performed on LMP and all LMFVP compositions in the range of 2.0−4.5 V vs Li/Li^+, applying a constant current, constant voltage (CCCV) test regime, with C-rates of C/2, 1C, 2C, and 5C being used during charge and discharge (where 1C value was assigned as 170 mA h g^{-1}), and holding the voltage used was 4.5 V (at the end of the charge step) until the current had decreased to 3% of the charge rate. Long-term cycling tests were performed subsequently at C/10, using the same holding voltage regime. The specific current and specific capacity was calculated based on the mass of active material (i.e., pure or doped $LiMnPO_4$) for each printed electrode.

■ ASSOCIATED CONTENT

Supporting Information

The Supporting Information is available free of charge on the ACS Publications website at DOI: 10.1021/acscombsci.6b00035.

Further experimental details, schematics of the continuous hydrothermal flow synthesis process, concentrations of precursors used in synthesis, Raman spectroscopy of the as-prepared and heat-treated powders, lattice parameter raw data for Figure 2, LeBail fits of XRD patterns of the materials for Figure 2, discharge capacity raw data for Figure 5, cyclic voltammetry data for each cell, and long-term cycling tests (PDF)

■ AUTHOR INFORMATION

Corresponding Author

*E-mail: j.a.darr@ucl.ac.uk. Office telephone: +44 (0)20 7679 4345. Fax: +44 (0)20 7679 7463. Mobile: +44 (0)7941 928875. Website: http://www.ucl.me.uk.

Author Contributions

The manuscript was written through contributions of all authors. All authors have given approval to the final version of the manuscript.

Notes

The authors declare no competing financial interest.

■ ACKNOWLEDGMENTS

EPSRC are thanked for funding the ELEVATE project (EP/M009394/1) and the Centre for Doctoral Training in Molecular Modelling & Materials Science (UCL, U.K.) which supports a studentship for Ian Johnson. The Warwick Manufacturing Group (WMG, University of Warwick, U.K.) are thanked for the use of their dry room and coin cell assembly equipment.

■ ABBREVIATIONS

LMP, $LiMnPO_4$; LFP, $LiFePO_4$; wt%, weight-percent; at%, atomic-percent; CHFS, continuous hydrothermal flow synthesis; LMFVP(*x*,*y*), $LiMn_{1-x-y}Fe_xV_yPO_4$; XRD, powder X-ray diffraction; JCPDS, Joint Committee on Powder Diffraction Standards; FE-SEM, field-emission scanning electron microscope; CV, cyclic voltammetry; confined jet mixer, CJM; PVDF, polyvinylidene fluoride; NMP, *N*-methyl-2-pyrrolidone; CCCV, constant current constant voltage

DOI: 10.1021/acscombsci.6b00035
ACS Comb. Sci. 2016, 18, 665−672

REFERENCES

(1) Padhi, A. K.; Nanjundaswamy, K. S.; Goodenough, J. B. Phospho olivines as Positive Electrode Materials for Rechargeable Lithium Batteries. *J. Electrochem. Soc.* **1997**, *144*, 1188−1194.

(2) Wang, Z. H.; Yuan, L. X.; Zhang, W. X.; Huang, Y. H. $LiFe_{0.8}Mn_{0.2}PO_4$/C cathode material with high energy density for lithium-ion batteries. *J. Alloys Compd.* **2012**, *532*, 25−30.

(3) Su, L.; Jing, Y.; Zhou, Z. Li ion battery materials with core-shell nanostructures. *Nanoscale* **2011**, *3* (10), 3967−3983.

(4) Nie, Z. X.; Ouyang, C. Y.; Chen, J. Z.; Zhong, Z. Y.; Du, Y. L.; Liu, D. S.; Shi, S. Q.; Lei, M. S. First principles study of Jahn−Teller effects in Li_xMnPO_4. *Solid State Commun.* **2010**, *150* (1−2), 40−44.

(5) Yamada, A.; Chung, S. C. Crystal chemistry of the olivine-type $Li(Mn_yFe_{1-y})PO_4$ and $(Mn_yFe_{1-y})PO_4$ as possible 4 V cathode materials for lithium batteries. *J. Electrochem. Soc.* **2001**, *148* (8), A960−A967.

(6) Blyr, A.; Sigala, C.; Amatucci, G.; Guyomard, D.; Chabre, Y.; Tarascon, J. M. Self-discharge of $LiMn_2O_4$/C Li-ion cells in their discharged state - Understanding by means of three-electrode measurements. *J. Electrochem. Soc.* **1998**, *145* (1), 194−209.

(7) Rangappa, D.; Sone, K.; Zhou, Y.; Kudo, T.; Honma, I. Size and shape controlled $LiMnPO_4$ nanocrystals by a supercritical ethanol process and their electrochemical properties. *J. Mater. Chem.* **2011**, *21* (39), 15813−15813.

(8) Wang, D.; Buqa, H.; Crouzet, M.; Deghenghi, G.; Drezen, T.; Exnar, I.; Kwon, N. H.; Miners, J. H.; Poletto, L.; Grätzel, M. High-performance, nano-structured $LiMnPO_4$ synthesized via a polyol method. *J. Power Sources* **2009**, *189* (1), 624−628.

(9) Zheng, J.; Ni, L.; Lu, Y.; Qin, C.; Liu, P.; Wu, T.; Tang, Y.; Chen, Y. High-performance, nanostructure $LiMnPO_4$/C composites synthesized via one-step solid state reaction. *J. Power Sources* **2015**, *282*, 444−451.

(10) Yoo, H.; Jo, M.; Jin, B.-S.; Kim, H.-S.; Cho, J. Flexible Morphology Design of 3D-Macroporous $LiMnPO_4$ Cathode Materials for Li Secondary Batteries: Ball to Flake. *Adv. Energy Mater.* **2011**, *1* (3), 347−351.

(11) Kwon, N.; Fromm, K. Enhanced electrochemical performance of < 30nm thin $LiMnPO_4$ nanorods with a reduced amount of carbon as a cathode for lithium ion batteries. *Electrochim. Acta* **2012**, *69*, 38−44.

(12) Wang, D.; Ouyang, C.; Drézen, T.; Exnar, I.; Kay, A.; Kwon, N.-H.; Gouerec, P.; Miners, J. H.; Wang, M.; Grätzel, M. Improving the Electrochemical Activity of $LiMnPO_4$ Via Mn-Site Substitution. *J. Electrochem. Soc.* **2010**, *157*, A225−A229.

(13) Martha, S. K.; Grinblat, J.; Haik, O.; Zinigrad, E.; Drezen, T.; Miners, J. H.; Exnar, I.; Kay, A.; Markovsky, B.; Aurbach, D. $LiMn_{0.8}Fe_{0.2}PO_4$: An Advanced Cathode Material for Rechargeable Lithium Batteries. *Angew. Chem., Int. Ed.* **2009**, *48* (45), 8559−8563.

(14) Sun, Y.-K.; Oh, S.-M.; Park, H.-K.; Scrosati, B. Micrometer-Sized, Nanoporous, High-Volumetric-Capacity $LiMn_{0.85}Fe_{0.15}PO_4$ Cathode Material for Rechargeable Lithium-Ion Batteries. *Adv. Mater.* **2011**, *23* (43), 5050−5054.

(15) Chen, M.-S.; Wu, S.-H.; Pang, W. K. Effects of vanadium substitution on the cycling performance of olivine cathode materials. *J. Power Sources* **2013**, *241*, 690−695.

(16) Harrison, K. L.; Bridges, C. A.; Paranthaman, M. P.; Segre, C. U.; Katsoudas, J.; Maroni, V. A.; Idrobo, J. C.; Goodenough, J. B.; Manthiram, A. Temperature Dependence of Aliovalent-Vanadium Doping in $LiFePO_4$ Cathodes. *Chem. Mater.* **2013**, *25* (5), 768−781.

(17) Lin, H.; Wen, Y. W.; Zhang, C. X.; Zhang, L. L.; Huang, Y. H.; Shan, B.; Chen, R. A GGA+U study of lithium diffusion in vanadium doped $LiFePO_4$. *Solid State Commun.* **2012**, *152* (12), 999−1003.

(18) Omenya, F.; Chernova, N. A.; Upreti, S.; Zavalij, P. Y.; Nam, K. W.; Yang, X. Q.; Whittingham, M. S. Can Vanadium Be Substituted into $LiFePO_4$? *Chem. Mater.* **2011**, *23* (21), 4733−4740.

(19) Zhang, L.; Liang, G.; Ignatov, A.; Croft, M.; Xiong, X.-Q.; Hung, I.-M.; Hu, X.-L.; Zhang, W.-X.; Peng, Y.-L.; et al. Effect of Vanadium Incorporation on Electrochemical Performance of $LiFePO_4$ for Lithium-Ion Batteries. *J. Phys. Chem. C* **2011**, *115*, 13520−13527.

(20) Dai, E.; Fang, H.; Yang, B.; Ma, W.; Dai, Y. Synthesis of vanadium doped $LiMnPO_4$ by an improved solid-state method. *Ceram. Int.* **2015**, *41* (6), 8171−8176.

(21) Wang, F.; Yang, J.; NuLi, Y.; Wang, J. Composites of $LiMnPO_4$ with $Li_3V_2(PO_4)_3$ for cathode in lithium-ion battery. *Electrochim. Acta* **2013**, *103*, 96−102.

(22) Zhang, J.-F.; Wang, X.-W.; Zhang, B.; Peng, C.-L.; Tong, H.; Yang, Z.-H. Multicore-shell carbon-coated lithium manganese phosphate and lithium vanadium phosphate composite material with high capacity and cycling performance for lithium-ion battery. *Electrochim. Acta* **2015**, *169*, 462−469.

(23) Barker, J.; Saidi, M. Y.; Swoyer, J. L. Lithium Iron(II) Phospho-olivines Prepared by a Novel Carbothermal Reduction Method. *Electrochem. Solid-State Lett.* **2003**, *6*, A53−A55.

(24) Hong, S. A.; Kim, S. J.; Kim, J.; Lee, B. G.; Chung, K. Y.; Lee, Y. W. Carbon coating on lithium iron phosphate ($LiFePO_4$): Comparison between continuous supercritical hydrothermal method and solid-state method. *Chem. Eng. J.* **2012**, *198*, 318−326.

(25) Chen, J.; Vacchio, M. J.; Wang, S.; Chernova, N.; Zavalij, P. Y.; Whittingham, M. S. The hydrothermal synthesis and characterization of olivines and related compounds for electrochemical applications. *Solid State Ionics* **2008**, *178*, 1676−1693.

(26) Gruar, R. I.; Tighe, C. J.; Darr, J. A. Scaling-up a Confined Jet Reactor for the Continuous Hydrothermal Manufacture of Nanomaterials. *Ind. Eng. Chem. Res.* **2013**, *52* (15), 5270−5281.

(27) Adschiri, T.; Kanazawa, K.; Arai, K. Rapid and Continuous Hydrothermal Crystallization of Metal Oxide Particles in Supercritical Water. *J. Am. Ceram. Soc.* **1992**, *75* (4), 1019−1022.

(28) Quesada-Cabrera, R.; Weng, X.; Hyett, G.; Clark, R. J. H.; Wang, H. Z.; Darr, J. A. High-Throughput Continuous Hydrothermal Synthesis of Nanomaterials (Part II): Unveiling the As-Prepared $Ce_xZr_yY_zO_{2-\delta}$ Phase Diagram. *ACS Comb. Sci.* **2013**, *15*, 458−463.

(29) Weng, X.; Cockcroft, J. K.; Hyett, G.; Vickers, M.; Boldrin, P.; Tang, C. C.; Thompson, S. P.; Parker, J. E.; Knowles, J. C.; Rehman, I.; Parkin, I.; Evans, J. R. G.; Darr, J. A. High-throughput continuous hydrothermal synthesis of an entire nanoceramic phase diagram. *J. Comb. Chem.* **2009**, *11*, 829−834.

(30) Kellici, S.; Gong, K.; Lin, T.; Brown, S.; Clark, R. J. H.; Vickers, M.; Cockcroft, J. K.; Middelkoop, V.; Barnes, P.; Perkins, J. M.; Tighe, C. J.; Darr, J. A. High-throughput continuous hydrothermal flow synthesis of Zn-Ce oxides: unprecedented solubility of Zn in the nanoparticle fluorite lattice. *Philos. Trans. R. Soc., A* **2010**, *368*, 4331−49.

(31) Goodall, J. B. M.; Illsley, D.; Lines, R.; Makwana, N. M.; Darr, J. A. Structure−Property−Composition Relationships in Doped Zinc Oxides: Enhanced Photocatalytic Activity with Rare Earth Dopants. *ACS Comb. Sci.* **2015**, *17* (2), 100−112.

(32) Goodall, J. B. M.; Kellici, S.; Illsley, D.; Lines, R.; Knowles, J. C.; Darr, J. A. Optical and photocatalytic behaviours of nanoparticles in the Ti-Zn-O binary system. *RSC Adv.* **2014**, *4* (60), 31799−31809.

(33) Gruar, R. I.; Tighe, C. J.; Muir, J.; Kittler, J. T.; Wodjak, M.; Kenyon, A. J.; Darr, J. A. Continuous hydrothermal synthesis of surface-functionalised nanophosphors for biological imaging. *RSC Adv.* **2012**, *2* (26), 10037−10047.

(34) Alexander, S. J.; Lin, T.; Brett, D. J. L.; Evans, J. R. G.; Cibin, G.; Dent, A.; Sankar, G.; Darr, J. A. A combinatorial nanoprecursor route for direct solid state chemistry: Discovery and electronic properties of new iron-doped lanthanum nickelates up to $La_4Ni_2FeO_{10-\delta}$. *Solid State Ionics* **2012**, *225*, 176−181.

(35) Dunne, P. W.; Starkey, C. L.; Gimeno-Fabra, M.; Lester, E. H. The rapid size- and shape-controlled continuous hydrothermal synthesis of metal sulphide nanomaterials. *Nanoscale* **2014**, *6* (4), 2406−2418.

(36) Hakuta, Y.; Seino, K.; Ura, H.; Adschiri, T.; Takizawa, H.; Arai, K. Production of phosphor (YAG:Tb) fine particles by hydrothermal synthesis in supercritical water. *J. Mater. Chem.* **1999**, *9*, 2671−2674.

(37) Adschiri, T.; Lee, Y.-W.; Goto, M.; Takami, S. Green materials synthesis with supercritical water. *Green Chem.* **2011**, *13*, 1380−1390.

DOI: 10.1021/acscombsci.6b00035
ACS Comb. Sci. 2016, 18, 665−672

(38) Hakuta, Y.; Onai, S.; Terayama, H.; et al. Production of ultrafine ceria particles by hydrothermal synthesis under supercritical conditions. *J. Mater. Sci. Lett.* **1998**, *17*, 1211−1213.
(39) Aimable, A.; Muhr, H.; Gentric, C.; Bernard, F.; Le Cras, F.; Aymes, D. Continuous hydrothermal synthesis of inorganic nanopowders in supercritical water: Towards a better control of the process. *Powder Technol.* **2009**, *190* (1−2), 99−106.
(40) Hong, S.-A.; Kim, S. J.; Chung, K. Y.; Chun, M.-S.; Lee, B. G.; Kim, J. Continuous synthesis of lithium iron phosphate ($LiFePO_4$) nanoparticles in supercritical water: Effect of mixing tee. *J. Supercrit. Fluids* **2013**, *73*, 70−79.
(41) Xu, C.; Lee, J.; Teja, A. S. Continuous hydrothermal synthesis of lithium iron phosphate particles in subcritical and supercritical water. *J. Supercrit. Fluids* **2008**, *44* (1), 92−97.
(42) Johnson, I. D.; Lübke, M.; Wu, O. Y.; Makwana, N. M.; Smales, G. J.; Islam, H. U.; Dedigama, R. Y.; Gruar, R. I.; Tighe, C. J.; Scanlon, D. O.; Corà, F.; Brett, D. J. L.; Shearing, P. R.; Darr, J. A. Pilot-scale continuous synthesis of a vanadium-doped $LiFePO_4$/C nanocomposite high-rate cathodes for lithium-ion batteries. *J. Power Sources* **2016**, *302*, 410−418.
(43) Islam, M.; Driscoll, D.; Fisher, C.; Slater, P. Atomic-scale investigation of defects, dopants, and lithium transport in the $LiFePO_4$ olivine-type battery material. *Chem. Mater.* **2005**, *17*, 5085−5092.
(44) Ma, J.; Li, B. H.; Du, H. D.; Xu, C. J.; Kang, F. Y. The Effect of Vanadium on Physicochemical and Electrochemical Performances of $LiFePO_4$ Cathode for Lithium Battery. *J. Electrochem. Soc.* **2011**, *158* (1), A26−A32.
(45) Doi, T.; Yatomi, S.; Kida, T.; Okada, S.; Yamaki, J. I. Liquid-phase synthesis of uniformly nanosized $LiMnPO_4$ particles and their electrochemical properties for lithium-ion batteries. *Cryst. Growth Des.* **2009**, *9* (12), 4990−4992.
(46) Lutterotti, L.; Matthies, S.; Wenk, H.-R., MAUD (Material Analysis Using Diffraction): A user friendly Java program for Rietveld Texture Analysis and more. In *Twelfth International Conference on Textures of Materials (ICOTOM-12)*; Szpunar, J. A., Eds.; NRC Research Press, McGill University: Montreal, Canada, 1999; Vol. 2, 1599.

DOI: 10.1021/acscombsci.6b00035
ACS Comb. Sci. 2016, 18, 665−672